Polarization-Dependent Scanning Photoionization Microscopy: Ultrafast Plasmon-Mediated Electron Ejection Dynamics in Single Au Nanorods

Volker Schweikhard, Andrej Grubisic, Thomas A. Baker, Isabell Thomann, and David J. Nesbitt*

JILA, University of Colorado, and National Institute of Standards and Technology, and Department of Chemistry and Biochemistry, University of Colorado, Boulder, Colorado 80309-0440, United States

ABSTRACT This work investigates plasmon-enhanced multiphoton scanning photoelectron emission microscopy (SPIM) of single gold nanorods under vacuum conditions. Striking differences in their photoemission properties are observed for nanorods deposited either on 2 nm thick Pt films or 10 nm thick indium tin oxide (ITO) films. On a Pt support, the Au nanorods display fourth-order photoionization when excited at 800 nm, a wavelength corresponding to their plasmon resonance in aqueous solution. A $\cos^8(\theta)$ dependence of the photoelectron flux on laser polarization implies photoemission mediated by the dipolar plasmon; however, no plasmon resonance signature is exhibited over the 750−880 nm range. Electromagnetic simulations confirm that the resonance is severely broadened compared to aqueous solution, indicative of *strong* interactions between the Au nanorod and propagating surface plasmon modes in the Pt substrate. On ITO substrates, by way of contrast, sharp plasmon resonances in the photoemission from individual Au nanorods are observed, with widths limited only by fundamental internal electron collision processes. Furthermore, the ensemble-averaged plasmon resonance for Au nanorods on ITO is almost unshifted compared to its frequency in solution. Both findings suggest that *plasmonic* particle−substrate interactions are suppressed in the Au/ITO system. However, Au nanorods on ITO exhibit a surprising *third*-order photoemission (observed neither in Au nor ITO by itself), indicating that *electrostatic* interactions introduce a substantial shift in the work function for this fundamental nanoparticle−substrate system.

KEYWORDS: plasmon resonance · multiphoton photoemission · photoelectron emission · gold nanorod · ultrafast electron dynamics · polarization dependence

Plasmon excitations on metal nanoparticles give rise to strong absorption and scattering resonances typically in the visible/UV region of the spectrum and allow the concentration of optical electric fields to the nanoscale far below the diffraction limit. For anisotropic particles, such as the rods studied herein, the plasmon resonance splits into an almost unshifted (with respect to spheres of the same diameter) transverse plasmon and an intense, red-shifted, longitudinal resonance (Figure 1a). An analytical formula for ellipsoidal Drude metal particles much smaller than the wavelength of light (see Schmucker *et al.*[1]) predicts resonance frequencies $\omega_{res} = \omega_{pl}/(1 + \varepsilon_d(1 - L)/L)^{1/2}$. Here, $\omega_{pl} = ((ne^2)/(\varepsilon_0 m_e))^{1/2}$ is the bulk plasma frequency,[2,3] n is the conduction electron density, e (m_e) is the electron's charge (mass), ε_0 is the dielectric permittivity of free space, and ε_d is the dielectric constant of the host material. The depolarization factor L depends on the ellipsoid's aspect ratio; for a rod oriented parallel to the laser polarization, $0 < L < 1/3$, resulting in a red-shifted frequency compared to a sphere ($L = 1/3$). Plasmonic metal particles can thus act as frequency-tunable and polarization-sensitive nanoscale antennas for light.[4−9] Due to their strong field localization and high sensitivity to the environment, plasmonic excitations may therefore provide a convenient optical interface between the macroscopic world and the nanoscale,[8,10,11] with applications ranging from information technologies[12−14] to low-volume, high-sensitivity sensing,[15−19] or the enhancement of absorption in photodetectors and photovoltaic devices.[20] Two types of nanostructures (*i.e.*, nanoshells[21−23] and nanorods)[24−32] have received particular interest in this respect, as their plasmon resonances can be tuned throughout the visible/near-infrared region by either optimizing the nanoshell thickness or nanorod aspect ratio.

In early studies on rough metal films and films of metal nanoparticles, it was soon recognized that plasmonic resonances not only dominate the optical properties of nanoparticles but also can exert pronounced effects on their photoionization dynamics.[33−37] Thus, optical studies of plasmon resonances can be complemented by highly sensitive experimental photoionization techniques. For example, photoelectron emission

* Address correspondence to djn@jila.colorado.edu.

Received for review January 8, 2011 and accepted April 5, 2011.

Published online April 05, 2011
10.1021/nn200082j

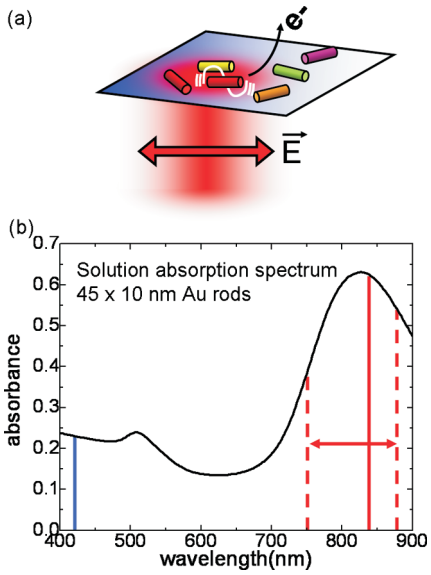

Figure 1. (a) Conceptual depiction of the experimental setup. Randomly oriented Au rods act as dipolar antennas with resonance frequencies in the optical regime. Multiphoton photoemission is initiated in a diffraction-limited excitation laser spot. The sample is scanned across the focal point, thus yielding a photoelectron emission image. Only rods whose long-axis dipolar plasmon oscillation frequency is resonant with the excitation frequency and whose orientation is well-aligned with the linear laser polarization will be excited and thus emit photoelectrons efficiently. (b) Solution absorption spectrum of 45 × 10 nm^2 Au rods, featuring the strong dipolar plasmon resonance around 830 nm.

microscopy (PEEM) has been used successfully to image patterned metal films and metal clusters[38] to reveal the spatial plasmon mode profiles in metal nanowires[39] and to follow the dynamics of localized plasmon modes on silver[40] and silver gratings.[41,42]

Coherent plasmon excitations in the visible spectral range are short-lived and therefore spectrally broad: electron−electron collisions[31] cause the decay of collective plasmon oscillations to single-particle excitations (electron−hole pairs) within tens of femtoseconds. In very small particles ($d \leq 10$ nm), surface scattering reduces the dephasing time even further.[43] For larger particles than the ones studied here, radiation damping (*i.e.*, light scattering) becomes increasingly important and dominates in particles larger than ~50−100 nm. This fact makes particles that support plasmons interesting not only in applications where they play a critical role as absorbers but also when they act as emitters, for example, to enhance the fluorescence quantum yield of poor dipolar emitters.[44] Efficient coupling between emitters and plasmons has recently been demonstrated at the level of single quanta by converting single quantum dot excitons to individual plasmon quanta and finally to single photons with a high efficiency.[12,13]

Another important emerging application of plasmonics is surface-enhanced Raman scattering (SERS),[45−48] where both the absorption and the emission process benefit from the strong plasmonic field localization/enhancement near nanoparticle surfaces, provided that the Raman shift energy difference between the initial and final state is within the plasmon bandwidth. In contrast with fluorescence/absorption enhancement processes, the virtual excited state is too short-lived for efficient energy transfer to occur, and as a result, there is no excited state nonradiative decay due to loss channels in the metal. SERS signal magnification of many orders of magnitude has been achieved, enabling detection at the single-particle level. In order to obtain reproducible SERS results and to establish SERS as a widely applicable technique, there is a growing interest in developing SERS substrates with a controlled geometry.

Understanding the impact of the local environment on the particle near-field and learning to control it is essential for continued advancement of all plasmon-based applications. Thus, detailed single-particle studies focusing on the influence of metal particle shape, size, and morphology on the strength of the local emitter−plasmon coupling, the scattering properties, and SERS activity would be greatly beneficial. In recent single-particle work, we and others have shown that multiphoton photoionization studies provide important information on single metal nanoparticles that complement those obtained from optical studies.[39,41,49−51] In this work, we focus on the effects of plasmon resonances on multiphoton photoemission from single, supported Au nanorods.

The paper is organized as follows. In Scanning Multiphoton Photoionization Microscopy (SPIM) of Single Nanorods, we present a brief description of the experiment. This is followed in Au Nanorods on Pt Thin Film Substrates by photoemission results for Au nanorods on 2 nm Pt film, which display the correct polarization ($\cos^8(\theta)$) and intensity (I^4) dependences expected for four-photon dipolar photoemission but do not exhibit plasmon resonances within the laser tuning range. In contrast, Au Rods on ITO Thin Film Substrates: Sharp Plasmon Resonances and Evidence for a Surface-Induced Work Function Shift presents results from Au nanorods supported by 10 nm ITO films, for which strong plasmon resonances are observed and can be analyzed in terms of fundamental e-scattering limits. As discussed further in the Discussion section, photoemission from Au rods on ITO displays a clear third-order dependence on laser intensity, despite a fourth-order power dependence observed from each of the constituents, Au and ITO, alone. Finally, Summary and Conclusions summarizes results as well as directions for further research exploration.

Scanning Multiphoton Photoionization Microscopy (SPIM) of Single Nanorods. In this work, SPIM is employed as a single-particle detection technique to complement single-particle fluorescence and light scattering studies, with the basic experimental approach depicted

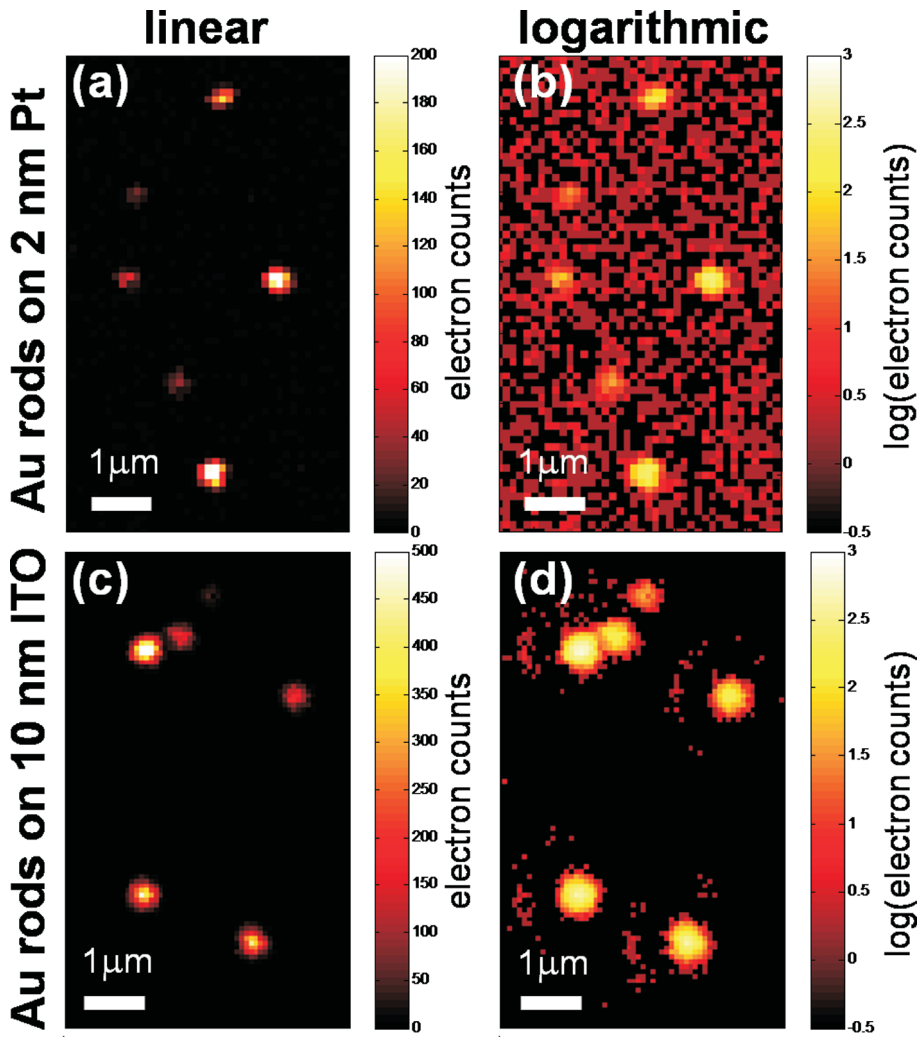

Figure 2. Scanning photoionization images of Au rods on 2 nm Pt (a,b) and Au rods on 10 nm ITO (c,d). Left: linear scale. Right: logarithmic scale. Au rods are observable as bright, diffraction-limited spots. Differences in intensity between rods arise from either frequency mismatch between plasmon resonance and laser excitation, the rod's noncollinear orientation with respect to the laser polarization, or intrinsic differences in the emission properties of individual rods. The log scale images reveal a dramatically increased signal-to-background ratio for Au rods on ITO *vs* Au rods on Pt.

conceptually in Figure 1a. Samples of Au rods are deposited onto a conducting substrate with rod axes parallel to the plane, but with random orientation in this plane. The surface density of rods is low enough that they can be individually excited with an ultrafast laser pulse brought to a diffraction-limited focus. Since the Au rods act as polarization-sensitive resonant antennas for light, only those rods whose long-axis dipolar plasmon oscillation frequency is resonant with the excitation frequency and whose axis is sufficiently aligned with the linear laser polarization will be excited and thus emit photoelectrons efficiently.

A scanning photoionization image of Au nanorods on 2 nm Pt film is shown in Figure 2a,b, while a SPIM image of Au nanorods on 10 nm ITO is displayed in Figure 2c,d. Rods are excited in the vicinity of the plasmon resonance frequency observed in aqueous solution using linearly polarized light at 840 nm. Au rods are visible on both substrates as diffraction-limited spots of high electron emissivity. The fact that they are observable above the photoemission background from the substrate already indicates that they are very "bright" emitters because they occupy only a tiny fractional area ($<10^{-3}$) of the focal spot. Considerable variations in emissivity between rods on the same substrate, apparent in Figure 2, arise from (1) noncollinear orientation of the rod axis with respect to the laser polarization, from (2) a frequency mismatch between the plasmon resonance frequency and the laser excitation frequency, as well as from (3) intrinsic differences in emission properties between rods. Furthermore, the logarithmic scale images (b) and (d) reveal a uniform background emissivity from the Pt substrate, while on ITO, the images are essentially background-free. It will be demonstrated that the substantial difference in contrast between Au nanorods and the two substrates is due, at least in part, to the presence (absence) of fast energy transfer

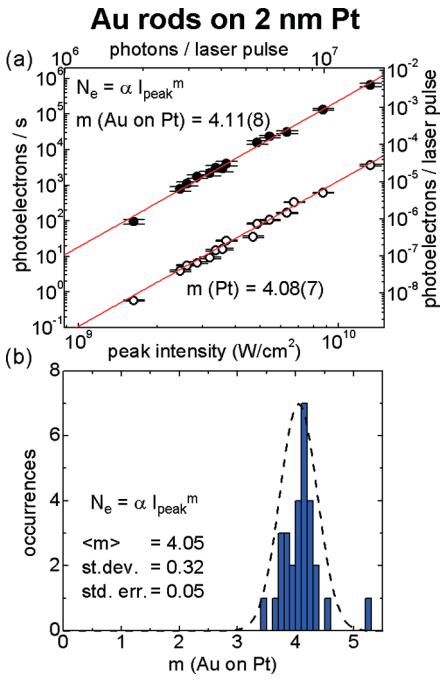

Figure 3. (a) Photoemission from an individual, representative Au rod on 2 nm Pt substrate (solid symbols) and from Pt substrate (hollow symbols) as a function of laser intensity. In both cases, a fourth-order intensity dependence is observed. (b) Distribution of best fit intensity-dependent exponents (*m*) in the measured power law behavior for an ensemble of 29 Au rods on Pt substrate reveals a mean (standard error) *m* = 4.05(5). The Pt substrate exhibits ~100-fold lower emissivity than the Au rods.

pathways from the Au rods to the Pt (ITO) substrate. In what follows, the photoemission mechanism, the role of the plasmon resonance, and several prominent differences in the photoemission from Au nanorods on these two substrates are examined in detail.

Au Nanorods on Pt Thin Film Substrates. Photoemission from Au nanorods on a 2 nm thick Pt substrate exhibits a fourth-order dependence on the intensity of the 840 nm laser excitation (see Figure 3a). An identical fourth-order dependence, albeit with a 100 times smaller signal level, is observed at the same wavelength for the Pt substrate itself (see Figure 3a). The statistics of the photoemission intensity dependence, $N_e \propto I_{peak}^m$, for an ensemble of 29 rods are summarized in Figure 3b, which yields a mean (standard error) intensity power dependence of m = 4.05(5). The obtained value is consistent with the minimum number (m = 4) of 840 nm photons (~1.5 eV) required to photoionize either gold ($\Phi \sim 5.2$ eV) or platinum ($\Phi \sim 5.5$ eV). The experimentally measured values of intensity power dependence for systems studied in this work are presented in Table 1.

It is instructive to quantify multiphoton photoemission by a multiphoton photoemission cross section *per unit emitter area* β_m, defined by the expression $N_e = \beta_m (I_{peak}/h\nu)^m A \tau_P$, where N_e is the number of photoemitted electrons per laser shot, $I_{peak}/h\nu$ is the peak

TABLE 1. Intensity (I_{peak}) Dependence $N_e \sim I_{peak}^m$ of Photoemission for Au Rods on Pt, Au Rods on ITO, and the 2 nm Pt and 10 nm ITO Substrates[a]

	Au rods on Pt	Au rods on ITO	Pt	ITO
intensity dependence m	4.05(5), N = 29	3.09(4), N = 16	4.08(7)	4.11(4)
polarization dependence n	8.9(4), N = 22	6.3(3), N = 21	—/—	—/—

[a] Polarization (θ) dependence $N_e \sim \cos(\theta - \theta_0)^n$ for Au rods on Pt and Au rods on ITO, given as the mean, with the standard error listed in parentheses, in units of the least significant figure. *N*: number of rods in an ensemble.

excitation photon flux (photons/s/area), m is the order of the emission process, and τ_P is the laser pulse duration. Here we define A as the relevant emitter area for each photoemissive material, that is, either the rod area itself ($A_{rod} = 45 \times 10$ nm^2 for nanoparticles) or the effective focal spot area for a 2D substrate, which based on an Airy pattern defined as $A_{foc} = \int I_{(r)}^m 2\pi r dr / I_{peak}^m = (1/m) \times (5.3 \times 10^{-9})$ cm^2; β_m is then simply related to the conventional multiphoton photoemission cross section by $\sigma_m = \beta_m \times A$. The photoemission coefficients β_m measured in this work are summarized in Table 2 and offer two valuable insights.

First of all, the four-photon photoemission coefficient for a 3 nm thick Au film evaporated on a 2 nm Pt substrate is $\beta_{4(Au\ films)} = 4(2) \times 10^{-94}$ cm^6 s^3, which is 400 times[50] stronger per unit area than the corresponding signals ($\beta_{4(Pt)} = 9(6) \times 10^{-97}$ cm^6 s^3) from the Pt substrate by itself. Second, this value of β_4 increases dramatically for Au rods *versus* 3 nm thick Au film, with $\beta_{4(Au\ rods)} = 1.7(9) \times 10^{-92}$ cm^6 s^3 now as much as $\approx 2 \times 10^4$ larger than the $\beta_{4(Pt)} = 9(6) \times 10^{-97}$ cm^6 s^3 values for the 2 nm Pt substrate itself. Finally, a comparison of $\beta_{4(Au\ rods)}$ and $\beta_{4(Au\ films)}$ shows that the magnitude of fourth-order photoemission β_4 from Au rods is ~50 times enhanced compared to photoemission from Au films. It is this combination of (i) nanorod *versus* thin film enhancement of photoemission as well as (ii) the inherently stronger emissivity of bulk gold compared to Pt that allows the observation of Au rods with high S/N contrast above the photoemission background from the conducting Pt films.

The elongated rod shape and the dominance of the dipolar plasmon resonance in the linear absorption spectrum at the employed excitation wavelengths both suggest that the photoemission intensity should be strongly polarization-dependent. Such effects have indeed been observed in earlier work on gold nanowires fabricated by e-beam lithography.[39] To explore the polarization dependence of photoionization in Au rods, sequences of SPIM images are recorded at different laser polarization angles θ. Figure 4a shows a typical polarization dependence of photoemission from two sample Au rods on Pt. The strong dependence of electron emission on polarization angle is apparent in the fact that the Au rod at the bottom emits

TABLE 2. Emitter-Area-Normalized Multiphoton Photoemission Coefficients β_m (Defined in the Text) for All Systems Studied: Au Rods on ITO, the 10 nm ITO Substrate, Au Rods on Pt, the 2 nm Pt Substrate, and 3 nm Bulk Au Films on ITO[a]

	β_4 (10^{-90} cm^6 s^3) (840 nm)	β_3 (10^{-60} cm^4 s^2) (840 nm)	β_2 (10^{-30} cm^2 s) (420 nm)
Au rods on ITO	—/—	0.5(2)	—/—
10 nm ITO substrate	$3(2) \times 10^{-10}$	—/—	$2.2(6) \times 10^{-9}$
Au rods on Pt	$1.7(9) \times 10^{-2}$	—/—	—/—
2 nm Pt substrate	$9(6) \times 10^{-7}$	—/—	$8(3) \times 10^{-7}$
3 nm Au on Pt	$4(2) \times 10^{-4}$	—/—	$8(3) \times 10^{-6}$

[a] Error bars are estimates, dominated by systematic uncertainty in the focal spot area, the pulse energy, and duration, as well as the electron collection efficiency.

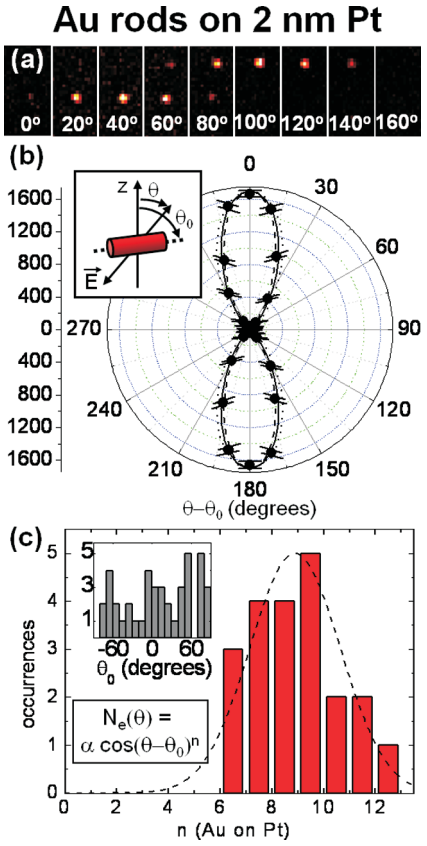

Figure 4. (a) Laser polarization dependence of photoemission from an ensemble of Au rods on 2 nm Pt. To merge the ensemble data into a single plot, emission from individual rods was fitted independently to a $\cos^n(\theta-\theta_0)$ functional form, thus determining the orientation θ_0 of each rod's long axis. (b) Ensemble statistics for the exponent value *n* in the polarization dependence. (c) Ensemble of 22 rods shows a mean (standard error) polarization dependence *n* = 8.9(4). A $\cos^8(\theta-\theta_0)$ dependence is consistent with the excitation of a purely dipolar plasmon and a fourth-order intensity dependence of photoelectron emission. Inset: ensemble statistics of rod orientations θ_0.

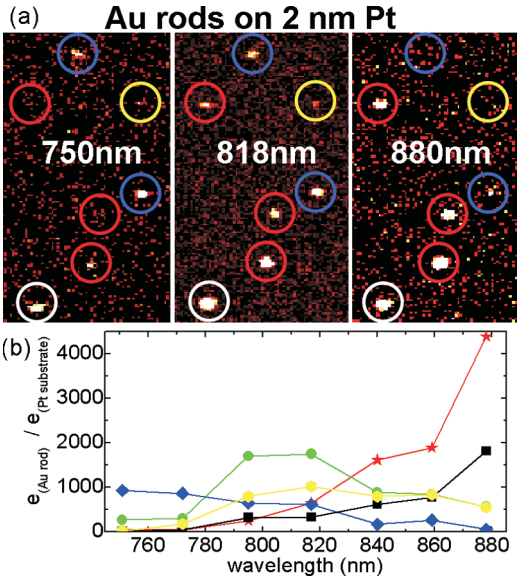

Figure 5. Excitation wavelength dependence of photoemission from Au rods on 2 nm Pt. (a) For most rods, the spectral dependence is broad and smooth; many rods (white) are visible over the entire accessible wavelength range. For some rods, emissivity increases to either long (red circles) or short wavelengths (blue). (b) Emissivity $\varepsilon_{(\text{Au rod})}$ *vs* wavelength for several representative rods (normalized by the emission from the Pt substrate, $\varepsilon_{(\text{Pt substrate})}$).

strongly near $\theta = 40°$, while the one in the top half emits most strongly around $\theta = 100°$. The orientations (θ_0) of individual rods are statistically distributed, as demonstrated in the inset of Figure 4c. To merge the ensemble data into a single plot, the emission from individual rods is first fitted to the form $\cos^n(\theta-\theta_0)$, thereby determining the rod orientation θ_0. With θ_0 established, the measured signals from an ensemble of randomly oriented rods can be averaged; in Figure 4b, the solid line indicates a $\cos^8(\theta-\theta_0)$ fit dependence, with the additional dashed and dotted lines representing best fits for $n = 6$ and 10, respectively. The measured ensemble statistics for 22 rods (see Figure 4c) show a polarization dependence $\cos^n(\theta-\theta_0)$ with a mean (standard error) exponent of $n = 8.9(4)$.

The observed polarization-dependent behavior is consistent with a strong contribution of the dipolar plasmon resonance to the photoemission process. It is thus reasonable to expect that a resonance structure may be apparent in the dependence of photoemission on excitation wavelength. The photoemission from Au rods on Pt as a function of the excitation wavelength within the tuning range of our Ti:sapphire laser (750−880 nm) is investigated in Figure 5. The data are obtained on Au rods with dimensions of 38 nm length × 10 nm diameter, which in aqueous solution exhibit a plasmon resonance at 780 nm and a 1σ width

of 50 nm. A series of SPIM images of the same sample area at different excitation wavelengths (Figure 5a) qualitatively demonstrate the observed wavelength-dependent photoemission. For some rods, it is found to increase with increasing wavelength, whereas for others, it decreases with increasing wavelength. The data for several representative individual Au rods on Pt are quantitatively shown in Figure 5b. For most rods, the spectral dependence of photoemission appears broader than our tuning range. A quantitative analysis of the data fails to produce an unambiguous signature of a plasmon resonance for the majority of rods. This measurement was repeated with several samples of different-size Au rods that have solution absorption maxima between 850 and 760 nm. In all cases, the ensemble-averaged emissivity consistently revealed the absence of a resonance in our tuning range and a slight upward trend with increasing wavelength. As presented later (see Discussion), electromagnetic simulations confirm that the plasmon resonance is broadened beyond recognition for Au rods on Pt, caused at least in part by strong interactions between the Au rod plasmon resonance and traveling surface plasmon waves supported by the Pt substrate.

Au Rods on ITO Thin Film Substrates: Sharp Plasmon Resonances and Evidence for a Surface-Induced Work Function Shift. To further elucidate the effects of a possible coupling of the Au rod plasmon resonance to surface plasmons in the substrate, the Pt substrate was substituted with an indium tin oxide (ITO) film, which does not support surface plasmon waves in the wavelength region of interest. In reflectance spectroscopy measurements, the reflectivity of the ITO thin film is found to be low throughout the visible spectrum but increases sharply below 8000−10 000 cm^{-1}, indicating a plasma frequency $\hbar\omega_{plasma} \sim 1-1.2$ eV.[52] The spectrum of surface plasmon excitations in ITO is thus expected to terminate at $\hbar\omega_{plasma}/\sqrt{2} \sim 0.8$ eV,[10] that is, far outside the region of the present study. ITO has a work function $\Phi \sim 4.7$ eV and is thus expected to give rise to fourth-order photoemission, which should facilitate comparison to the results obtained on Pt. As shown in Figure 6a, the ITO substrate (hollow symbols) indeed shows the expected fourth-order dependence on laser intensity with a remarkably low emissivity ($\beta_4 = 3(2) \times 10^{-100}$ cm^6 s^3), that is, an additional 4000-fold lower than the 2 nm Pt substrate.

However, photoemission from single 45 nm × 10 nm Au rods on the ITO substrate (solid symbols) exhibits a third-order rather than the expected fourth-order power dependence on laser intensity (Figure 6a). Statistics on an ensemble of Au rods on ITO confirm the generality of this behavior (Figure 6b). The ensemble of 16 rods shows an intensity dependence $N_e \propto I_{peak}^m$, with a mean (standard error) $m = 3.09(4)$, although a third-order power dependence is displayed by neither Au nor ITO independently. Furthermore, for a third-order

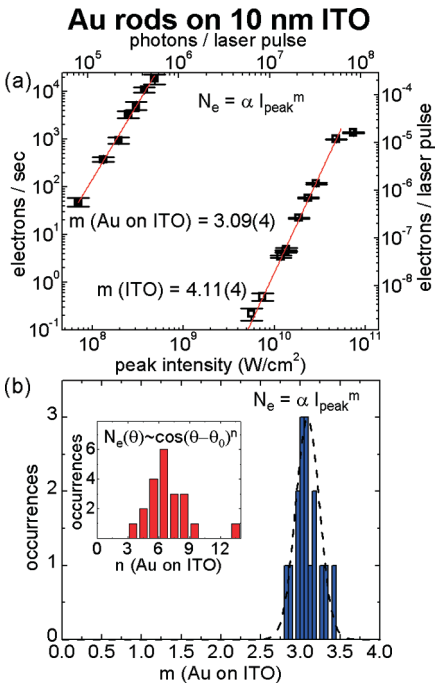

Figure 6. Au rods on 10 nm ITO. (a) Photoemission from an individual, representative Au rod on 10 nm ITO substrate (solid symbols) and from ITO substrate alone (hollow symbols) as a function of laser intensity. Surprisingly, only a third-order power dependence is observed for individual Au rods, whereas the ITO exhibits the expected fourth-order intensity dependence and a markedly lower emissivity. (b) Distribution of exponent values *m*, in the measured power law behavior $N_e = \alpha I_{peak}^m$ (with a constant α) for an ensemble of 16 Au rods on ITO, showing a mean (standard error) $m = 3.09(4)$. Inset: polarization dependence of photoemission from Au rods on ITO ($\cos^n(\theta-\theta_0)$, with $n = 6.3(3)$), is consistent with third-order emission from a dipolar source.

photoemission process from a dipolar source, one would expect a $\cos^6(\theta-\theta_0)$ polarization dependence of emission. Interestingly, this surprising third-order photoemission process is also supported by polarization-dependent photoemission studies of Au rods on ITO, which for an ensemble of 21 rods reveals a $\cos^n(\theta-\theta_0)$ polarization dependence with a mean (standard error) $n = 6.3(3)$.

The wavelength-dependent photoemission behavior of Au rods deposited on ITO *versus* Pt thin film substrates is observed to be quite different, as well. Unlike Au rods on Pt, the photoemission from Au rods on an ITO substrate exhibits well-defined, narrow plasmon resonances (Figure 7). Resonance peaks are statistically distributed across the 750−880 nm excitation range and display widths from 30 to 60 nm, as shown in Figure 7b. Almost half of all rods display a resonance that falls outside of this excitation range. This broad distribution of resonance wavelengths is consistent with the broad (~700−900 nm) resonance observed in the solution absorption spectrum (Figure 1b) and suggests that the bulk absorption profile is strongly affected by inhomogeneous broadening.

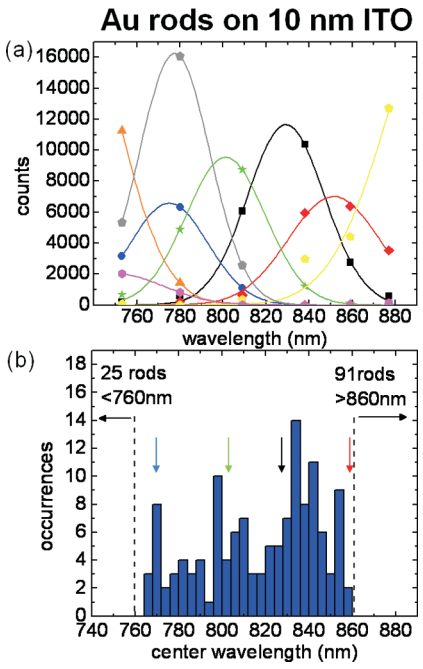

Figure 7. (a) Photoemission from individual Au rods on 10 nm ITO as a function of wavelength exhibits pronounced plasmon resonances. Resonance wavelengths are statistically distributed across the entire 750−880 nm excitation range of the Ti:sapphire laser and beyond. (b) Ensemble statistics of plasmon resonance wavelengths. The distribution is wider than the tuning range of the excitation source.

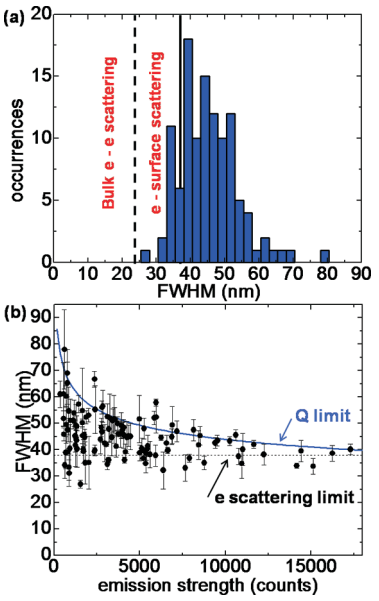

Figure 8. (a) Observed distribution of plasmon resonance widths (fwhm) for Au rods on 10 nm ITO, together with two theoretical limits given by fundamental dephasing processes, *i.e.*, bulk electron−electron collisions and electron−surface collisions. (b) Correlation of fwhm and emission strength. The brightest rods are probably aligned with the laser polarization and also likely exhibit strong intrinsic emissivity. Rods of lower brightness may be either intrinsically weaker emitters or not collinearly oriented with the laser polarization axis. The "*Q*-limit" (blue curve, normalized to the brightest peak) assumes that the emissivity is related to the *Q*-factor of the plasmon resonance (see text). Rods near this curve represent the sample heterogeneity of resonance *Q*-factors. The 10 brightest rods show a very consistent narrow fwhm of 37.9(9) nm (dotted line). Plasmon lifetimes in rods close to this e-scattering limit are dominated by fundamental dephasing processes; differences in their emission strengths are mainly due to orientation with respect to the laser polarization.

Further effects of sample heterogeneity are evident in the distribution of single-particle plasmon resonance widths (shown in Figure 8a), which ranges from $\Delta\lambda \sim 30$ to $\sim$70 nm. The upper value is twice as large as the fundamental limit set by dephasing of the plasmon by electron−electron and electron−surface scattering processes (see below),[27] suggesting that at least in some rods additional broadening mechanisms are responsible. To investigate this heterogeneous behavior further, we explore in Figure 8b the correlation between (i) the fwhm of the plasmon resonance and (ii) the peak photoemission strength, for single Au nanorods on 10 nm ITO at the peak plasmon resonance and fixed laser polarization. Specifically, the most strongly emitting rods consistently exhibit the narrowest line widths, with the average fwhm of the 10 brightest rods at $\Delta\lambda \approx 37.9(9)$ nm (dotted line in Figure 8b). On the other hand, a much larger spread in fwhm (from $\Delta\lambda \sim$ 30 to $\sim$70 nm) is observed for the less emissive rods.

These data suggest that diminished photoemissivity signals correlate with an intrinsically lower *Q*-factor ($Q = \omega_0$/fwhm) of the plasmon resonance, for example, caused by defects in the crystalline structure of a rod. More quantitatively, the plasmonic field should grow with consecutive cycles of the excitation laser until $E \sim QE_0$, where E_0 is the field after a single laser oscillation. For a third-order (I^3) photoemission process, the emission strength is thus expected to vary with $Q^6 \sim$ fwhm^{-6}; consequently, one predicts the fwhm to scale as (emission strength)$^{-1/6}$. This trend is indicated by the blue curve in Figure 8b and fits the upper envelope of the observed data rather well. Conversely, low emissivity may be exhibited by rods that are relatively defect-free (*i.e.*, large *Q*-factors and consequently narrow line widths) but are not aligned with the laser polarization axis, thereby explaining the observed spread in fwhm for rods with low emission strengths. No rods exhibit significantly narrower fwhm than that of the brightest ones. Thus, the *Q*-limit and the fundamental "electron scattering limit" fully describe the "phase space" of allowed combinations of emission strength and line width.

DISCUSSION

Intensity Dependence of Photoemission. For structures exhibiting a strong plasmonic field enhancement, photoionization is generally thought to proceed *via* (i) excitation of a strong collective plasmon oscillation of the electron gas as a whole, followed by (ii) transfer of sufficient energy to a single electron to promote it to the vacuum level. In earlier work, Lehmann *et al.*

deduced that coherent multiphoton absorption is the dominant process in Ag particles that are excited near their plasmon resonance at 400 nm.[34] Given the work functions of Au ($\Phi_{Au} \sim 5.2$ eV), Pt ($\Phi_{Pt} \sim 5.5$ eV), and ITO ($\Phi_{ITO} \sim 4.7$ eV) a *four*-photon photoionization is expected for all three materials when excited by 840 nm light (1.5 eV). With the exception of Au rods on ITO, the observed power law dependence of photoemission on laser intensity (see Table 1) is consistent with the literature values for the work functions of the respective materials. In contrast, the surprising I^3 and $\cos^6(\theta)$ dependence in the case of Au rods on ITO demands further explanation. Note that two observations suggest that significant saturation of the plasmon response can be immediately ruled out: (1) No change in the power law dependence on excitation intensity is observed for Au rods on ITO throughout the entire range of laser intensities employed. (2) The experiments on ITO are conducted at 10-fold lower excitation intensity than experiments on Pt, where both the I^4 and the $\cos^8(\theta)$ dependences point to negligible saturation effects.

Multiphoton emission is not the only possible photoionization mechanism for nanoparticles. Thermionic emission[53] can play an important role, as found, for example, by Gloskovskii and co-workers for small Ag and Au particles (less than a few nanometers in size) excited by femtosecond pulses at 800 nm.[54] To estimate the role of thermionic emission for Au rods on ITO, we follow the treatment by Ekici *et al.*[55] and Gloskovskii *et al.*[54] to calculate a maximum electron temperature of 2300 K after excitation at the highest intensity used ($I_P = 5 \times 10^8$ W/cm^2). This temperature drops rapidly with lattice equilibration (*i.e.*, after $\tau_{cool} \sim$ 10 ps), yielding a duty cycle $\tau_{cool} \times f_{rep}$. With a current given by the Richardson–Dusham equation,[56,57] $I_{th} = A_{surf}A_0T^2\exp(-\Phi_{Au}/T)$ for $A_0 = 1.2 \times 10^6$ Am^{-2} K^{-2} and nanorod surface area A_{surf}, this predicts electron count rates of $I_{th} \times \tau_{cool} \times f_{rep} = 2000$ e/s at $I_P = 5 \times 10^8$ W/cm^2, that is, 1 order of magnitude lower than what we measure (*cf.* Figure 6a). A negligible role of thermionic emission from Au rods on ITO is further supported by our experiments on Pt, where pure multiphoton emission is observed even at 10-fold higher excitation intensity than on ITO. Both findings strongly suggest that multiphoton emission is the dominant process for our 45 × 10 nm^2 Au rods on ITO. Instead, we speculate that the unexpected *three*-photon photoionization of Au rods on ITO may be related to a modification of the work function of the ITO–Au rod adsorbate system. It is well-known that in the interaction of metal adsorbate electrons with their own image charge can drastically reduce the work function of the substrate/adsorbate system.[58] Given that ITO is not far from the threshold for three-photon photoemission when 840 nm light is employed, even a small work function modification can induce a change from four- to three-photon ionization. We anticipate that future theoretical studies will be able to shed more light on this intriguing possibility.

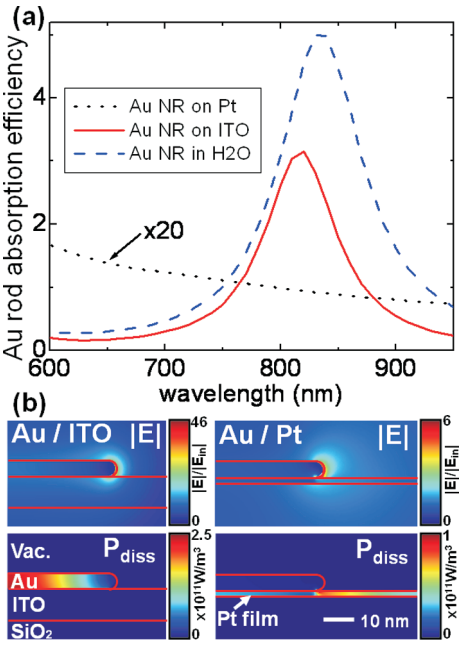

Figure 9. Finite-difference frequency domain (COMSOL) simulations of nanoparticle–plasmon–substrate coupling, approximating the nanorod/substrate in 2D and adjusting the Au rod's aspect ratio to recapitulate the observed nanorod plasmon resonance peak in H_2O (see text for details). (a) Simulated absorption efficiency (*i.e.*, the ratio of the rod's absorption cross section over its geometrical cross section) for Au nanorods in H_2O (dashed blue), on 10 nm ITO (solid red), and on 2 nm Pt (dotted black line, scaled up 20×). In H_2O and on ITO, *sharp* plasmon resonances are observed, with only a small (~20 nm) blue shift between ITO and H_2O. In stark contrast, however, no such resonance structure is observed for Au nanorods on Pt over the full simulation range from 450 to 950 nm. (b) To elucidate the lack of resonance behavior on Pt, the corresponding electric field ($|E|$, normalized by the incident field $|E_{in}|$) and dissipated power density (P_{diss}) distributions are shown. On both substrates, significant near-*E*-field concentration (~5 nm 1/*e* field decay length) is seen near the Au nanorod tips, though with ~7-fold lower absolute strength for Pt *versus* ITO. However, while dissipation on ITO occurs *inside* the Au rod, the vast majority of energy on Pt is transferred to the substrate and is dissipated there. Furthermore, a traveling surface plasmon wave is launched into the Pt film, guiding energy far beyond the nanorod enhanced near-field. The surface plasmon propagation length of ~40 nm ($1/e^2$ decay of the dissipated power) is well explained by losses due to interband transitions in Pt.[59] Ultrafast energy transfer to the surface plasmon in Pt thus broadens the Au nanorod plasmon resonance beyond our current tuning range.

Coupling between Nanoparticle Plasmons and Surface Plasmons on Pt Substrates. To interpret the lack of a plasmon resonance spectral signature on 2 nm Pt, we have performed additional electromagnetic simulations (see Materials and Methods) for each of our Au rod–substrate systems. The results, shown and explained in Figure 9, confirm the absence of any resonance feature for Au rods on Pt and provide clear evidence that, at least in part, the underlying

mechanism consists of (i) energy transfer from the Au rod to the Pt substrate and (ii) launching of a traveling surface plasmon wave in the Pt film, driven by the Au particle's near-fields close to its tips. However, an additional role of interband transitions in Pt in broadening the Au rod resonance cannot be ruled out.[59]

Strong nanoparticle−substrate coupling has also been observed for Au spheres on Au substrates by Mock and co-workers,[60] in their case leading to significant (up to 130 nm) red shifts of the plasmon resonance. Image dipole interactions can also induce red shifts for particles on dielectric substrates, albeit to a smaller extent, as demonstrated by the Halas group.[61] The lack of a significant frequency shift for Au rods on ITO (Figure 7), which also is supported by our simulations (Figure 9a), thus appears to be the consequence of mutually canceling effects of particle−*sub*strate interactions (inducing a red shift) and replacement of water with a vacuum "*super*strate" (inducing a blue shift).

Estimating Plasmonic Field Enhancements from Photoemission Data. Stronger photoemission is generally observed from Au rods than from a Au film when comparing photoemissivity on a per emitter area basis (β). The enhancement factor for four-photon emission in the case of Au rods on Pt is β_4(Au rods on Pt)/β_4(3 nm Au film on Pt) ≈ 50. If the field enhancement near the surface of a thin continuous Au film is assumed to be negligible, the plasmonic field enhancement in Au nanorods can be calculated from β_4(Au rods on Pt)/β_4(3 nm Au film on Pt) ≈ $(E_{loc}/E_{in})^8$, yielding an average local (E_{loc}) over incident field (E_{in}) ratio of $E_{loc}/E_{in} \sim 1.6$. Such a low value stands in strong contrast with field enhancement factors ∼50 typically encountered for plasmonic resonances. For example, Ropers and co-workers studied femtosecond four-photon photoemission from sharp metal tips and experimentally deduced that the local electric field at a tip with 20 nm radius of curvature is enhanced 10-fold.[62] Kelly and co-workers[63] used the discrete dipole approximation to estimate that at the surface of a resonantly excited 30 nm radius silver particle the electric field is enhanced by a factor of 50. The lack of any such dramatic field enhancement for Au rods on Pt in the present experiments further supports our interpretation that fast energy transfer to the Pt substrate prevents the buildup of a substantial near-field around the nanoparticle.

In contrast, Au rods on ITO exhibit much stronger emission and well-defined plasmon resonances in four-photon photoemission spectra consistent with negligible energy transfer to the substrate. Unfortunately, the electric field enhancement factor for the case of Au rods on ITO cannot be deduced in a similarly straightforward fashion as in the case of Au rods on Pt because the observed *three*-photon photoemission can not be compared with a bulk third-order photoionization cross section since bulk Au exhibits a *four*-photon photoemission in our excitation wavelength range. Nevertheless, an estimate of the enhancement factor can be obtained by comparing typical photoemission yields observed when exciting a particular Au nanorod both on and away from its plasmon resonance. The photoemission rate generally observed for Au nanorods on ITO at their plasmon resonance is N_e(on-resonance) ∼ 10^6 e^-/s, whereas for excitation ∼50 nm off-resonance they can often not be distinguished from the ITO background, thus yielding an upper limit for the photoemission rate, N_e(off-resonance) < 10^{-3} e^-/s. Consequently, a lower bound for the electric field enhancement factor can be determined from $(E_{loc}/E_{in})^6 = N_e$(on-resonance)/N_e(off-resonance) > 10^9, thus yielding $E_{loc}/E_{in} > 30$. This value is consistent with previously observed electric field enhancement factors[63] of ∼50, confirming the absence of strong energy transfer pathways to the ITO substrate that would prevent the buildup of significant plasmonic fields.

Plasmon Resonance Widths and Fundamental e^- Scattering Processes on ITO. Another factor influencing the photoemissivity of Au rods is the width of plasmon resonances observed in the four-photon photoemission spectra of Au rods on ITO. In particular, they exhibit an ensemble average fwhm of 41.6(6) nm, which after deconvolution from the 25 nm excitation laser bandwidth yields $\Delta\lambda \approx 34$ nm fwhm. The average fwhm of the 10 brightest rods is even narrower, 37.9(9) nm, yielding a deconvolved fwhm of $\Delta\lambda \approx 29$ nm. Since photoemission from Au nanorods on ITO is a three-photon process, we further scale the deconvolved fwhm by $\sqrt{3}$ in order to facilitate comparison with the values obtained from linear absorption and scattering experiments. The resulting effective "single-photon" fwhm determined from our experiment is 58 nm (100 meV) for the ensemble and 49 nm (85 meV) for the brightest rods.

In earlier light scattering work, line widths around 50 nm were observed for single Au rods with plasmon resonance frequencies below 1.8 eV, that is, below the absorption threshold for transitions from the occupied d-band to the conduction band.[31] Muskens *et al.*, in their work on the extinction cross sections of single Au rods with plasmon resonance wavelengths >700 nm, observed a fwhm of 40 nm (70 meV).[26] The most systematic study to date by Novo and co-workers found line widths of 63 nm (110 meV) in the case of 45 nm × 10 nm rods, which have been the focus of the present work, as well.[27]

For 45 × 10 nm rods, the dominant contribution to the plasmon line width is bulk scattering by electron−electron collisions ($\hbar\Gamma_{bulk}$ = 73 meV for gold in the 1−2 eV spectral region).[31,64] In addition, there is a non-negligible contribution from surface scattering, $\hbar\Gamma_{surface} \approx 35$ meV.[65] The total damping rate for the

Au rods studied in the present paper is thus given by $\hbar\Gamma \approx \hbar\Gamma_{bulk} + \hbar\Gamma_{surface} \approx 108$ meV. Radiation damping, measured by Sonnichsen *et al.* in studies of single spherical gold particles with sizes larger than 40 nm in diameter, is negligible for such small rods ($\hbar\Gamma \sim 1$ meV).[31] The fact that the damping rates calculated by theory agree well with experiments suggests that Au nanorods possess near perfect crystallinity and high surface quality, at least in the case of the most emissive rods. The increased damping observed for some of the less emissive rods may be a consequence of structural defects incurred during their synthesis or differences in the local nanorod−substrate coupling. For example, polycrystalline Ag nanowires exhibit significantly reduced plasmon *Q*-factors compared to single-crystalline ones.[66] The good agreement between the line widths measured in the present study and those obtained by theory and other, earlier experiments implies that additional contributions to damping, such as significant energy transfer to the ITO substrate, can be ruled out, at least in the case of the brightest Au rods.

SUMMARY AND CONCLUSIONS

Pronounced effects of plasmon resonances on the multiphoton photoemission propensity of Au rods on 10 nm ITO have been observed. Sharp plasmon resonances in multiphoton emission spectra exhibit spectral widths that appear to be limited only by fundamental processes, such as bulk electron−electron and electron−surface scattering. These findings are in good agreement with theory as well as with earlier optical studies. In contrast, plasmon resonances in photoemission are not observed in the case of Au rods on 2 nm Pt substrates, either due to a substantial (>100 nm) red shift of the resonance or due to a strong spectral broadening. Both effects are consistent with a strong interaction (energy transfer or dipole−dipole coupling) between the localized plasmons in the Au rods and surface plasmons supported by the substrate. The single-electron detection sensitivity of the instrument employed in these studies allows high signal-to-background information to be obtained even in such a case, where a strong plasmon resonant enhancement is likely absent. The findings suggest that plasmon-enhanced photoemission from Au nanorods can serve as a sensitive probe of the coupling between localized plasmon modes and their environment. Future work will be aimed at studying the coupling between plasmons and nearby molecules or semiconductor quantum dots *via* photoemission experiments.

MATERIALS AND METHODS

A 2 nm thick Pt layer was thermally evaporated onto glass coverslips (Corning No. 1 $^1/_2$) and had a sheet resistance of ~10 MΩ/sq.[1] The 10 nm thick ITO substrates, low-temperature sputtered onto glass coverslips (Corning No. 1 $^1/_2$), were purchased from Thin Film Devices, Inc. After 30 min of ozone cleaning, ITO sheet resistance was ~2 kΩ/sq. Cetyltrimethylammonium bromide (CTAB)-capped Au rods (45 × 10 nm) in aqueous solution were purchased from Nanopartz and used as received. Typically, 30 μL of stock solution containing ~10^{11} Au rods per milliliter were spin-coated on substrates at 1000 rpm. Following the sample preparation, the coverslips were immediately transferred into the vacuum chamber. The absorption spectrum of the aqueous solution of Au rods (Figure 1b) displayed the intense, *long-axis* dipolar plasmon resonance at 828 nm, with a 1σ width of 69 nm. The feature apparent at ~510 nm is the weaker *transverse* dipolar plasmon. The increasing absorption at wavelengths shorter than 500 nm arose from the excitation of interband transitions in gold.

The basic experimental setup for scanning photoionization microscopy (SPIM) has been described in detail previously.[67] Recent improvements in experimental sensitivity down to the single-electron counting level have been reported elsewhere.[50] Briefly, multiphoton photoemission was initiated in a near-diffraction limited femtosecond laser spot, generated by overfilling the back aperture of a reflective microscope objective *in vacuo* (numerical aperture, NA = 0.65). The sample was scanned across the fixed excitation spot, and an image of the local photoelectron emissivity was recorded. Individual electrons were registered using a channeltron electron multiplier and amplifier/discriminator setup, with an estimated 35% overall detection efficiency.[50] We used the output of a mode-locked Ti:sapphire laser (centered at 840 nm with a full width at half-max (fwhm) value of 24 nm), with an extra-cavity prism compensator providing compressed pulses at the sample focal area at a repetition rate f_{rep} = 85 MHz. For all calculations, we assumed a near-Fourier transform-limited pulse duration τ_P = 50 fs, focused to a diffraction-limited spot area $A = 1.2025 \times \text{fwhm}^2$, where fwhm = 0.515 × λ/NA ($A = 5.3 \times 10^{-9}$ cm^2 for NA = 0.65 and λ = 840 nm). Photoelectron emission is a multiphoton process, where the required minimum number of photons *n*, with energy E_{photon}, is given by the expression $n \times E_{photon} > \Phi$, where Φ is the work function of a particular material. Although the excitation conditions vary somewhat between the different samples examined and the illumination wavelength employed, typical operation yields a pulse energy of about $E_P \sim 0.4$ pJ/pulse, corresponding to ~1.7×10^6 "red" photons/pulse, focused to a peak intensity $I_{peak} \sim 1.54 \times 10^9$ W/cm^2. Under these circumstances, approximately 100 e^-/s (electrons per second) were detected from Au rods on 2 nm Pt, 0.5 e^-/s from the Pt substrate, 10^6 e^-/s from Au rods on 10 nm ITO, and 10^{-3} e^-/s from the ITO substrate.

We note that in our experiments the initial state prior to each photoionization events can be assumed to be a neutral Au nanorod. Specifically, all data are taken in the regime of <1% ionization probability per laser shot, with reneutralization through the conductive substrate occurring faster than the time between subsequent laser pulses. This is important to rule out because the plasmon resonance in charged metal nanoparticles could undergo a frequency blue shift that is proportional to the particle's charge state.[68]

Two-dimensional full-field electromagnetic simulations were performed using the finite-difference frequency domain method (COMSOL), which fully accounts for the frequency-dependent optical constants of the materials. Reflection symmetry allows restriction of the simulation domain to one-half of the structure. An adaptive mesh with element sizes of ~0.4 nm in and around the Au rod and ~15 nm in vacuum far away from the rod is used. To better match the results of our 2D simulations to our 3D observations, we adjusted the simulated rod

dimensions to match the simulated absorption peak in aqueous solution to the experimentally determined value of 830 nm. The resulting simulated rod dimensions were 70 nm length × 5 nm diameter, compared to the experimental values of 45 × 10 nm^2. We note that our electromagnetic simulations do not take into account additional phenomena such as charge transfer and charge transport.

Acknowledgment. This work has been supported by the Air Force Office of Scientific Research, with additional funds for optics, microscopy, and computer resources provided by the National Science Foundation and the National Institute for Standards and Technology.

REFERENCES AND NOTES

1. Schmucker, A. L.; Harris, N.; Banholzer, M. J.; Blaber, M. G.; Osberg, K. D.; Schatz, G. C.; Mirkin, C. A. Correlating Nanorod Structure with Experimentally Measured and Theoretically Predicted Surface Plasmon Resonance. *ACS Nano* **2010,** *4*, 5453–5463.
2. Bohren, C. F.; Huffman, D. R. *Absorption and Scattering of Light by Small Particles*; Wiley-VCH: Weinheim, Germany, 1983.
3. Pelton, M.; Aizpurua, J.; Bryant, G. Metal-Nanoparticle Plasmonics. *Laser Photonics Rev.* **2008,** *2*, 136–159.
4. Farahani, J.; Eisler, H.-J.; Pohl, D. W.; Hecht, B. Single Quantum Dot Coupled to a Scanning Optical Antenna: A Tunable Superemitter. *Phys. Rev. Lett.* **2005,** *95*, 017402.
5. Kuehn, S.; Hakanson, U.; Rogobete, L.; Sandoghdar, V. Enhancement of Single-Molecule Fluorescence Using a Gold Nanoparticle as an Optical Nanoantenna. *Phys. Rev. Lett.* **2006,** *97*, 017402.
6. Muehlschlegel, P.; Eisler, H.-J.; Martin, O. J. F.; Hecht, B.; Pohl, D. W. Resonant Optical Antennas. *Science* **2005,** *308*, 1607–1609.
7. Novotny, L. Effective Wavelength Scaling for Optical antennas. *Phys. Rev. Lett.* **2007,** *98*, 266802.
8. Schuck, P. J.; Fromm, D. P.; Sundaramurthy, A.; Kino, G. S.; Moerner, W. E. Improving the Mismatch between Light and Nanoscale Objects with Gold Bowtie Nanoantennas. *Phys. Rev. Lett.* **2005,** *94*, 017402.
9. Taminiau, T.; Stefani, F. D.; Segerink, F. B.; Van Hulst, N. F. Optical Antennas Direct Single-Molecule Emission. *Nat. Photonics* **2008,** *2*, 234–237.
10. Barnes, W. L.; Dereux, A.; Ebbesen, T. W. Surface Plasmon Subwavelength Optics. *Nature* **2003,** *424*, 824–830.
11. Lal, S.; Link, S.; Halas, N. J. Nano-optics from Sensing to Waveguiding. *Nat. Photonics* **2007,** *1*, 641–648.
12. Akimov, A. V.; Mukherjee, A.; Yu, C. L.; Chang, D. E.; Zibrov, A. S.; Hemmer, P. R.; Park, H.; Lukin, M. D. Generation of Singe Optical Plasmons in Metallic Nanowires Coupled to Quantum Dots. *Nature* **2007,** *450*, 402–406.
13. Chang, D. E.; Sorensen, A. S.; Hemmer, P. R.; Lukin, M. D. Quantum Optics with Surface Plasmons. *Phys. Rev. Lett.* **2006,** *97*, 053002.
14. Ozbay, E. Plasmonics: Merging Photonics and Electronics at Nanoscale Dimensions. *Science* **2006,** *311*, 189–193.
15. Anker, J. N.; Hall, W. P.; Lyandres, O.; Shah, N. C.; Zhao, J.; Van Duyne, R. P. Biosensing with Plasmonic Nanosensors. *Nat. Mater.* **2008,** *7*, 442–453.
16. Novo, C.; Funston, A. M.; Mulvaney, P. Direct Observation of Chemical Reactions on Single Gold Nanocrystals Using Surface Plasmon Spectroscopy. *Nat. Nanotechnol.* **2008,** *3*, 598–602.
17. Rosi, N. L.; Mirkin, C. A. Nanostructures in Biodiagnostics. *Chem. Rev.* **2005,** *105*, 1547–1562.
18. West, J. L.; Halas, N. J. Engineered Nanomaterials for Biophotonics Applications: Improving Sensing, Imaging, And Therapeutics. *Annu. Rev. Biomed. Eng.* **2003,** *5*, 285–292.
19. McFarland, A. D.; Van Duyne, R. P. Single Silver Nanoparticles as Real-Time Optical Sensors with Zeptomole Sensitivity. *Nano Lett.* **2003,** *3*, 1057–1062.
20. Pillai, S.; Catchpole, K. R.; Trupke, T.; Green, M. A. Surface Plasmon Enhanced Silicon Solar Cells. *J. Appl. Phys.* **2007,** *101*, 093105.
21. Bardhan, R.; Grady, N. K.; Cole, J. R.; Joshi, A.; Halas, N. J. Fluorescence Enhancement by Au Nanostructures: Nanoshells and Nanorods. *ACS Nano* **2009,** *3*, 744–752.
22. Halas, N. J. Playing with Plasmons: Tuning the Optical Resonant Properties of Metallic Nanoshells. *MRS Bull.* **2005,** *30*, 362–367.
23. Tanabe, K. Field Enhancement around Metal Nanoparticles and Nanoshells: A Systematic Investigation. *J. Phys. Chem. C* **2008,** *112*, 15721–15728.
24. Alekseeva, A. V.; Bogatyrev, V. A.; Khlebtsov, B. N.; Mel'nikov, A. G.; Dykman, L. A.; Khlebtsov, N. G. Gold Nanorods: Synthesis and Optical Properties. *Colloid J.* **2006,** *68*, 661–678.
25. Mohamed, M. B.; Volkov, V.; Link, S.; El-Sayed, M. A. The "Lightning" Gold Nanorods: Fluorescence Enhancement of over a Million Compared to the Gold Metal. *Chem. Phys. Lett.* **2000,** *317*, 517–523.
26. Muskens, O. L.; Bachelier, G.; Fatti, N. D.; Vallee, F.; Brioude, A.; Jiang, X.; Pileni, M.-P. Quantitative Absorption Spectroscopy of a Single Gold Nanorod. *J. Phys. Chem. C* **2008,** *112*, 8917–2981.
27. Novo, C.; Gomez, D.; Perez-Juste, J.; Zhang, Z.; Petrova, H.; Reismann, M.; Mulvaney, P.; Hartland, G. V. Contributions from Radiation Damping and Surface Scattering to the Linewidth of the Longitudinal Plasmon Band of Gold Nanorods: A Single Particle Study. *Phys. Chem. Chem. Phys.* **2006,** *8*, 3540–3546.
28. Orendorff, C. J.; Gearheart, L.; Janaz, N. R.; Murphy, C. J. Aspect ratio dependence on surface enhanced Raman scattering using silver and gold nanorod substrates. *Phys. Chem. Chem. Phys.* **2005,** *8*, 165–170.
29. Pelton, M.; Liu, M.; Kim, H. Y.; Smith, G.; Guyot-Sionnest, P.; Scherer, N. F. Optical Trapping and Alignment of Single Gold Nanorods by Using Plasmon Resonances. *Opt. Lett.* **2006,** *31*, 2075–2077.
30. Pelton, M.; Liu, M.; Park, S.; Scherer, N. F.; Guyot-Sionnest, P. Ultrafast resonant Optical Scattering from Single Gold Nanorods: Large Nonlinearities and Plasmon Saturation. *Phys. Rev. B* **2006,** *73*, 155419.
31. Sönnichsen, C.; Franzl, T.; Wilk, T.; von Plessen, G.; Feldmann, J.; Wilson, O.; Mulvaney, P. Drastic Reduction of Plasmon Damping in Gold Nanorods. *Phys. Rev. Lett.* **2002,** *88*, 077402.
32. Link, S.; El-Sayed, M. A. Spectral Properties and Relaxation Dynamics of Surface Plasmon Electronic Oscillations in Gold and Silver Nanodots and Nanorods. *J. Phys. Chem. B* **1999,** *103*, 8410–8426.
33. Evers, F.; Rakete, C.; Watanabe, K.; Menzel, D.; Freund, H. J. Two-photon photoemission from silver nanoparticles on thin alumina films: Role of plasmon excitation. *Surf. Sci.* **2005,** *593*, 43–48.
34. Lehmann, J.; Merschdorf, M.; Pfeiffer, W.; Thon, A.; Voll, S.; Gerber, G. Surface Plasmon Dynamics in Silver Nanoparticles Studied by Femtosecond Time-Resolved Photoemission. *Phys. Rev. Lett.* **2000,** *85*, 2921–2924.
35. Stuckless, J. T.; Moskovits, M. Enhanced Two-Photon Photoemission from Coldly Deposited Silver Films. *Phys. Rev. B* **1989,** *40*, 9997–9998.
36. Merschdorf, M.; Pfeiffer, W.; Thon, A.; Voll, S.; Gerber, G. Photoemission from Multiply Excited Surface Plasmons in Ag Nanoparticles. *Appl. Phys. A* **2000,** *71*, 547–552.
37. Kennerknecht, C.; Hövel, H.; Merschdorf, M.; Voll, S.; Pfeiffer, W. Surface Plasmon Assisted Photoemission from Au Nanoparticles on Graphite. *Appl. Phys. B* **2001,** *73*, 425–429.
38. Fecher, G. H.; Schmidt, O.; Hwu, Y.; Schonhense, G. Multiphoton Photoemission Electron Microscopy Using Femtosecond Laser Radiation. *J. Electron Spectrosc.* **2002,** *126*, 77.
39. Douillard, L.; Charra, F.; Korczak, Z.; Bachelot, R.; Kostcheev, S.; Lerondel, G.; Adam, P.-M.; Royer, P. Short Range

Plasmon Resonators Probed by Photoemission Electron Microscopy. *Nano Lett.* **2008,** *8*, 935–940.
40. Kubo, A.; Pontius, N.; Petek, H. Femtosecond Microscopy of Surface Plasmon Polariton Wave Packet Evolution at the Silver/Vacuum Interface. *Nano Lett.* **2007,** *7*, 470–475.
41. Kubo, A.; Onda, K.; Petek, H.; Sun, Z. J.; Jung, Y. S.; Kim, H. K. Ferntosecond Imaging of Surface Plasmon Dynamics in a Nanostructured Silver Film. *Nano Lett.* **2005,** *5*, 1123–1127.
42. Kubo, A.; Jung, Y. S.; Kim, H. K.; Petek, H. Femtosecond Microscopy of Localized and Propagating Surface Plasmons in Silver Gratings. *J. Phys. B: At. Mol. Opt. Phys.* **2007,** *40*, S259–S272.
43. Bosbach, J.; Hendrich, C.; Stietz, F.; Vartanyan, T.; Träger, F. Ultrafast Dephasing of Surface Plasmon Excitation in Silver Nanoparticles: Influence of Particle Size, Shape, and Chemical Surrounding. *Phys. Rev. Lett.* **2002,** *89*, 257404.
44. Mertens, H.; Koenderink, A. F.; Polman, A. Experimental Evidence for Large Dynamic Effects on the Plasmon Dispersion of Subwavelength Metal Nanoparticle Waveguides. *Phys. Rev. B* **2007,** *76*, 115123.
45. Brus, L. Noble Metal Nanocrystals: Plasmon Electron Transfer Photochemistry and Single-Molecule Raman Spectroscopy. *Acc. Chem. Res.* **2008,** *41*, 1742–1749.
46. Haes, A. J.; Haynes, C. L.; McFarland, A. D.; Schatz, G. C.; Van Duyne, R. R.; Zou, S. L. Plasmonic materials for surface-enhanced sensing and spectroscopy. *MRS Bull.* **2005,** *30*, 368–375.
47. Nie, S.; Emery, S. R. Probing Single Molecules and Single Nanoparticles by Surface-Enhanced Raman Scattering. *Science* **1997,** *275*, 1102–1106.
48. Talley, C. E.; Jackson, J. B.; Oubre, C.; Grady, N. K.; Hollars, C. W.; Lane, S. M.; Huser, T. R.; Nordlander, P.; Halas, N. J. Surface-Enhanced Raman Scattering from Individual Au Nanoparticles and Nanoparticle Dimer Substrates. *Nano Lett.* **2005,** *5*, 1569–1574.
49. Cinchetti, M.; Gloskovskii, A.; Nepijko, S. A.; Schoenhense, G.; Rochholz, H.; Kreiter, M. Photoemission Electron Microscopy as a Tool for the Investigation of Optical Near Fields. *Phys. Rev. Lett.* **2005,** *95*, 047601.
50. Schweikhard, V.; Grubisic, A.; Baker, T. A.; Nesbitt, D. J. Multiphoton Scanning Photoionization Imaging Microscopy for Single-Particle Studies of Plasmonic Metal Nanostructures. *J. Phys. Chem. C* **2011,** *115*, 83–91.
51. Wiemann, C.; Bayer, D.; Rohmer, M.; Aeschlimann, M.; Bauer, M. Local 2PPE-Yield Enhancement in a Defined Periodic Silver Nanodisk Array. *Surf. Sci.* **2007,** *601*, 4714–4721.
52. Brewer, S. H.; Franzen, S. Indium Tin Oxide Plasma Frequency Dependence on Sheet Resistance and Surface Adlayers Determined by Reflectance FTIR Spectroscopy. *J. Phys. Chem. B* **2002,** *106*, 12986–12992.
53. Grua, P.; Morreeuw, J. P.; Bercegol, H.; Jonusauskas, G.; Vallee, F. Electron Kinetics and Emission for Metal Nanoparticles Exposed to Intense Laser Pulses. *Phys. Rev. B* **2003,** *68*, 035424.
54. Gloskovskii, A.; Valdaitsev, D. A.; Cinchetti, M.; Nepijko, S. A.; Lange, J.; Aeschlimann, M.; Bauer, M.; Klimenkov, M.; Viduta, L. V.; Tomchuk, P. M.; Schonhense, G. Electron Emission from Films of Ag and Au Nanoparticles Excited by a Femtosecond Pump-Probe Laser. *Phys. Rev. B* **2008,** *77*, 195427.
55. Ekici, O.; Harrison, R. K.; Durr, N. J.; Eversole, D. S.; Lee, M.; Ben-Yakar, A. Thermal Analysis of Gold Nanorods Heated with Femtosecond Laser Pulses. *J. Phys. D: Appl. Phys.* **2008,** *41*, 185501.
56. Crowell, C. R. Richardson Constant and Tunneling Effective Mass for Thermionic and Thermionic-Field Emission in Schottky Barrier Diodes. *Solid-State Electron.* **1969,** *12*, 55–59.
57. Crowell, C. R. Richardson Constant for Thermionic Emission in Schottky Barrier Diodes. *Solid-State Electron.* **1965,** *8*, 395–399.
58. Zhao, J.; Pontius, N.; Winkelmann, A.; Sametoglu, V.; Kubo, A.; Borisov, A. G.; Sanchez-Portal, D.; Silkin, V. M.; Chulkov, E. V.; Echenique, P.; Petek, H. Electronic Potential of a Chemisorption Surface. *Phys. Rev. B* **2008,** *78*, 085419.
59. Rakic, A. D.; Djurisic, A. B.; Elazar, J. M.; Majewski, M. L. Optical Properties of Metallic Films for Vertical-Cavity Optoelectronic Devices. *Appl. Opt.* **1998,** *37*, 5271–5283.
60. Mock, J. J.; Hill, R. T.; Degiron, A.; Zauscher, S.; Chilkoti, A.; Smith, D. R. Distance-Dependent Plasmon Resonant Coupling between a Gold Nanoparticle and Gold Film. *Nano Lett.* **2008,** *8*, 2245–2252.
61. Knight, M. W.; Wu, Y.; Lassiter, J. B.; Nordlander, P.; Halas, N. J. Substrates Matter: Influence of an Adjacent Dielectric on an Individual Plasmonic Nanoparticle. *Nano Lett.* **2009,** *9*, 2188–2192.
62. Ropers, C.; Solli, D. R.; Schulz, C. P.; Lienau, C.; Elsaesser, T. Localized Multiphoton Emission of Femtosecond Electron Pulses from Metal Nanotips. *Phys. Rev. Lett.* **2007,** *98*, 043907.
63. Kelly, K. L.; Coronado, E.; Zhao, L. L.; Schatz, G. C. The Optical Properties of Metal Nanoparticles: The Influence of Size, Shape, and Dielectric Environment. *J. Phys. Chem. B* **2003,** *107*, 668–677.
64. Palik, E. D. *Handbook of Optical Constants of Solids*; Academic Press: New York, 1985.
65. Berciaud, S.; Cognet, L.; Tamarat, P.; Lounis, B. Observation of Intrinsic Size Effects in the Optical Response of Individual Gold Nanoparticles. *Nano Lett.* **2005,** *5*, 515–518.
66. Ditlbacher, H.; Hohenau, A.; Wagner, D.; Kreibig, U.; Rogers, M.; Hofer, F.; Aussenegg, F. R.; Krenn, J. R. Silver Nanowires as Surface Plasmon Resonators. *Phys. Rev. Lett.* **2005,** *95*, 257403.
67. Monti, O. L. A.; Baker, T. A.; Nesbitt, D. J. Imaging Nanostructures with Scanning Photoionization Microscopy. *J. Chem. Phys.* **2006,** *125*, 154709.
68. Mulvaney, P.; Perez-Juste, J.; Giersig, M.; Liz-Marzan, L. M.; Pecharroman, C. Drastic Surface Plasmon Mode Shifts in Gold Nanorods Due to Electron Charging. *Plasmonics* **2006,** *1*, 61–66.